Article:

Alharbi, A.H., Alzahrani, M.S.J., Moslem, W.M. et al. (2026) Ion-neutral coupled electrostatic solitary waves in the Martian dayside M1 ionosphere. Monthly Notices of the Royal Astronomical Society, 550 (2). stag1262. ISSN: 0035-8711

https://doi.org/10.1093/mnras/stag1262

Ion-Neutral Coupled Electrostatic Solitary Waves in the Martian Dayside M1 Ionosphere

A. H. Alharbi *,[1], M. S. J. Alzahrani ,[2], W. M. Moslem ,[3,4], I. Ballai [5], and I. S. Elkamash ,[4,6]

[1] Mathematics Department, Faculty of Sciences, Umm Al-Qura University, Makkah 21955, Saudi Arabia
[2]Mechanical and Industrial Engineering Department, College of Engineering and Computing– Al-Leith, Umm Al-Qura University, Makkah 25375, Saudi Arabia
[3] Physics Department, Faculty of Science, Port Said University, Port Said 42521, Egypt
[4]Centre for Theoretical Physics, The British University in Egypt, Shorouk City 11837, Egypt
[5]Plasma Dynamics Group (PDG), School of Mathematical and Physical Sciences, The University of Sheffield, Hicks Building, Hounsfield Road, Sheffield, S3 7RH, United Kingdom
[6]Physics Department, Faculty of Science, Mansoura University, Mansoura 35516, Egypt

Abstract

The lower dayside ionosphere of Mars, corresponding to the M1 layer, is a weakly ionized and strongly collisional plasma region in which ion–neutral coupling is expected to strongly influence the evolution of electrostatic disturbances. However, direct waveform measurements in this altitude range remain limited. We investigate the nonlinear evolution of small-amplitude electrostatic ion-acoustic solitary structures in the Martian dayside M1 ionosphere and assess how plasma and neutral parameters control their propagation, attenuation, and observability under representative conditions constrained by observations from the Mars Atmosphere and Volatile EvolutioN (MAVEN) mission. Starting from a multi-fluid Boltzmann–Poisson model for O_2^+ ions, Boltzmann electrons, and a CO_2-dominated neutral gas, we use the reductive perturbation method to derive a variable-coefficient Korteweg–de Vries equation with weak collisional attenuation. Here, the variable coefficients represent the dependence of the nonlinear, dispersive, stratification, and effective attenuation terms on the slowly varying M1 plasma–neutral background. The small-amplitude qualification refers to the asymptotic ordering used in the reductive-perturbation derivation, while the resulting solitary pulse remains intrinsically nonlinear. The results show that the intrinsic pulse shape is mainly controlled by the

*E-mail: ahhrbe@uqu.edu.sa

nonlinear and dispersive coefficients, whereas the pulse lifetime and possible detectability are controlled primarily by effective ion–neutral attenuation and neutral co-motion. Attenuation decreases with altitude; ion temperature makes the electrostatic pulses narrower and faster; neutral temperature has only a weak effect; and neutral density plays only a limited role in the co-moving case, while neutral co-motion provides the broadest range of behaviours, from strong attenuation to nearly adiabatic propagation. The co-moving M1 parameter sets satisfy the weak-attenuation criterion and permit a quantitatively controlled adiabatic solitary-pulse description, whereas the immobile-neutral limit violates this criterion for the representative pulse considered and is retained only as a qualitative upper bound on collisional attenuation. The electrostatic pulse has an electric-field amplitude of about 0.017 $\mathrm{mV\,m^{-1}}$, a frequency range of 6–7 kHz, and a duration of the order of 10^{-3} s. These predicted signatures provide observational targets for a future low-altitude Mars mission equipped with high-sensitivity, high-cadence electric-field waveform measurements and simultaneous plasma and neutral diagnostics.

1 Introduction

Partially ionized plasmas (PIPs) are prevalent—indeed, effectively ubiquitous—throughout the solar system and in a broad range of astrophysical environments. In PIPs, a substantial neutral component interacts with charged species through momentum exchange, modifying transport and wave dynamics via Cowling (enhanced) resistivity, ambipolar diffusion driven by electron-pressure gradients, and finite ion–neutral drift [1–4]. Representative environments include the lower ionospheres of terrestrial planets (e.g., Mars and Venus), Titan's extended ionosphere, dense cometary comae, and plume-fed regions such as Enceladus' torus. In these systems, strong ion–neutral collisional coupling plays a dominant role in controlling wave propagation, momentum transport, and energy dissipation. On Venus, radio occultation measurements have identified a lower V1 layer (approximately 120–135 km) and a newly characterized V0 layer (at altitudes of $\lesssim$ 120 km) in which collisional processes are dominant [5]. Titan displays substantial Pedersen and Hall conductivities, as well as an altitude-dependent coupling to the ambient magnetospheric plasma flow [6]. Cometary comae, such as that of 67P/Churyumov–Gerasimenko, constitute weakly ionized natural laboratories in which freshly produced heavy molecular ions undergo frequent collisions with a dense neutral background, thereby governing the development of ambipolar electric fields, ion pickup dynamics, and a diverse spectrum of plasma-wave activity [7, 8]. Furthermore, plume-dominated environments (e.g., Enceladus) generate dense, collisionally controlled regions characterized by strong ion–neutral chemistry and complex electrodynamic interactions [9]. The relative importance of collisionality and magnetization is conveniently measured by the ratio ν_{in}/Ω_{ci} of the ion–neutral collision frequency to the ion gyrofrequency. When $\nu_{in} \gtrsim \Omega_{ci}$, collisional coupling suppresses Hall dynamics and favours an electrostatic, fluid-like response on ion-acoustic timescales [1, 2]. Because neutral densities and scale heights vary significantly with altitude and solar forcing, PIPs frequently display gradual inhomogeneity, which must be accounted for in electrostatic-wave modelling [1, 3, 4].

Over the past decade, observations from the Mars Atmosphere and Volatile EvolutioN (MAVEN) mission have substantially improved our understanding of the structure, variability, and fine-scale organization of the Martian lower dayside ionosphere. For example, radio occultation measurements from the MAVEN Radio Occultation Science Experiment (ROSE) have provided vertically resolved electron-density profiles through the M1 and M2 ionospheric layers and revealed how the lower ionosphere responds to changing solar illumination and ambient atmospheric conditions [10]. Indeed, the M1 region is typically located at altitudes of $\sim$ 95–135 km, below the dominant M2 layer. The M1 layer comprises a weakly ionized plasma immersed in a neutral background composed primarily of CO_2 and CO. Therefore, plasma transport and wave evolution are expected to be strongly modulated by ion–neutral collisions, neutral-wind forcing, and ambipolar electrodynamics [11–13]. Furthermore, the Langmuir Probe and Waves (LPW) instrument provides *in situ* plasma diagnostics, including electron density, electron temperature, and electric-field spectral measurements. Comparisons between the ROSE and LPW datasets show that they are mostly consistent and help to define the observational regimes in which each instrument gives the most reliable constraints [14, 15]. MAVEN has also shown that the lower Martian ionosphere is not a vertically smooth plasma layer, but it frequently exhibits structured ion-density irregularities, indicating that this region supports dynamically organized plasma variability [16, 17].

Direct waveform measurements of electrostatic structures in the M1 altitude range remain limited because no mission has yet been designed to perform dedicated low-altitude wave measurements in this strongly collisional layer [10, 14, 18, 19]. At the same time, electrostatic solitary structures have been observed or modelled in several planetary-plasma environments, including the Martian magnetosheath, Martian reconnection-exhaust regions, electronegative Martian plasma, and lunar wake plasma [20–24]. Although these studies provide important context for our work, they mainly address collisionless or weakly collisional regions, or arbitrary-amplitude Sagdeev-type structures. The lower dayside Martian M1 ionosphere is different because it is weakly ionized, highly collisional, and vertically structured, so that ion–neutral momentum exchange and neutral co-motion can strongly affect the evolution and detectability of electrostatic perturbations. This observational limitation motivates the central question of the present study: if small-amplitude nonlinear electrostatic ion-acoustic solitary disturbances form in the lower M1 ionosphere, can they survive its weakly ionized and strongly collisional conditions, and which plasma–neutral parameters control their amplitude, width, speed, lifetime, and possible detectability? The fundamental motivation is to determine how ion–neutral coupling modifies the nonlinear ion-acoustic balance between nonlinear steepening and Debye-scale dispersion. The small-amplitude qualification refers to the asymptotic ordering used in the reductive-perturbation method and does not imply that the resulting solitary pulse is linear or nearly linear.

Accordingly, we use the standard reductive-perturbation/KdV framework not as a new mathematical technique, but as a reduced theoretical-fluid diagnostic model for small-amplitude nonlinear electrostatic ion-acoustic solitary pulses in a vertically structured, collisional M1 plasma. Here, variable coefficient means that the nonlinear, dispersive, stratification, and attenuation coefficients depend on slowly varying plasma and neutral parameters, including density, temperature, altitude stratification, and ion–neutral coupling. The attenuation considered here is temporal attenuation in the slow co-moving coordinate, caused by ion–neutral momentum exchange, rather than an imposed spatial damping coefficient. When the solution is transformed back to physical space and time, this attenuation represents amplitude loss during pulse propagation, thereby connecting the stretched-coordinate description to observable pulse duration, width, speed, electric-field amplitude, and frequency scale. The specific advance of the present work is therefore the adaptation of the variable-coefficient KdV model with weak collisional attenuation to MAVEN/Viking-constrained M1 conditions. Within one reduced framework, we include oxygen molecular ions, a carbon-dioxide-dominated neutral background, weak stratification, ion temperature, ion–neutral momentum exchange, and partial neutral co-motion. This allows us to show that nonlinear and dispersive effects mainly determine the intrinsic pulse shape, whereas effective ion–neutral attenuation and neutral co-motion control the survival and detectability of the pulse in the lower Martian ionosphere.

The observational significance of these structures is primarily diagnostic rather than technological. The M1 layer is a poorly sampled transition between the dense neutral atmosphere and the less collisional upper ionosphere, where ion–neutral momentum exchange, vertical stratification, and plasma compressibility act simultaneously. If localized electrostatic ion-acoustic pulses were detected, their amplitude, duration, width, propagation speed, and attenuation rate could provide indirect constraints on the local collisional relaxation rate and the degree of neutral co-motion. The present model therefore identifies an altitude- and coupling-dependent observational window rather than predicting uniformly favourable propagation throughout the M1 layer. The predicted observational signatures consist of weak bipolar electric-field pulses with amplitudes of approximately 0.016–0.017 $\mathrm{mV\,m^{-1}}$, durations of order 10^{-3} s, and characteristic spectral power near 6–7 kHz. Testing these predictions would require a future low-altitude Mars mission carrying a high-sensitivity electric-field waveform receiver with a sampling rate in the tens-of-kilohertz range, together with simultaneous measurements of electron density and temperature, ion composition, and neutral density and composition. Such coordinated measurements would allow the observed pulse properties and attenuation rate to be compared directly with the local plasma–neutral coupling regime.

The structure of this paper is organized as follows. In Section 2, we present the theoretical fluid model for electrostatic ion-acoustic perturbations in the lower Martian M1 ionosphere. In Section 3, we derive the variable-coefficient KdV equation with weak collisional attenuation and discuss its solitary-pulse solution, including the relation between stretched and physical coordinates. In Section 4, we analyse the parameter regimes controlling pulse shape, attenuation, lifetime, and possible observability. Finally, Section 5 summarizes the main findings and conclusions.

2 Theoretical model

We consider a one-dimensional electrostatic plasma composed of ions (i), neutrals (n), and Boltzmann electrons, where electron inertia is neglected. Ion and electron pressure effects, ion–neutral momentum exchange, and Poisson coupling are taken into account. Here, n_i, n_n, and n_e denote the normalized ion, neutral, and electron number densities, respectively, while u_i and u_n denote the normalized ion and neutral fluid velocities. The subscripts i, n, and e refer to ions, neutrals, and electrons, respectively.

The variables are normalized using the ion–acoustic speed $C_s = \sqrt{k_B T_e/m_i}$ as the velocity scale, the electron thermal potential $\Phi = k_B T_e/e$ as the potential scale, the Debye length $\lambda_D = \sqrt{\varepsilon_0 k_B T_e/(n_{i0} e^2)}$ as the length scale, and the ion plasma period $t_* = \omega_{pi}^{-1}$ as the time scale, where $\omega_{pi} = \sqrt{n_{i0} e^2/(\varepsilon_0 m_i)}$ is the ion plasma frequency. In these definitions, k_B is Boltzmann's constant, T_e is the electron temperature, m_i is the ion mass, e is the elementary charge, ε_0 is the vacuum permittivity, and n_{i0} is the equilibrium ion density used in the normalization. The variables x and t below are therefore normalized by λ_D and ω_{pi}^{-1}, respectively. Hereafter, ϕ denotes the normalized electrostatic potential, whereas Φ denotes only the dimensional potential scale used for normalization.

With the above normalization, the normalized multi-fluid–Boltzmann–Poisson system reads

$$\partial_t n_i + \partial_x(n_i u_i) = 0, \tag{1}$$

$$\partial_t n_n + \partial_x(n_n u_n) = 0, \tag{2}$$

$$\partial_t u_i + u_i \partial_x u_i = -\partial_x \phi - \sigma_i \partial_x(\ln n_i) - \nu_{in}^*(u_i - u_n) + G, \tag{3}$$

$$\partial_t u_n + u_n \partial_x u_n = -\sigma_n \partial_x(\ln n_n) - \nu_{ni}^*(u_n - u_i) + G, \tag{4}$$

$$\partial_x^2 \phi = e^{\phi} - n_i, \qquad n_e = e^{\phi}. \tag{5}$$

Throughout the manuscript, ∂_t and ∂_x denote partial differentiation with respect to the normalized time t and normalized spatial coordinate x, respectively. The momentum–transfer symmetry condition is

$$m_i n_{i0}\, \nu_{in}^* = m_n n_{n0}\, \nu_{ni}^*. \tag{6}$$

In Eq. (6), m_n is the neutral-particle mass, n_{n0} is the equilibrium neutral density, ν_{in}^* is the normalized ion–neutral collision frequency, and ν_{ni}^* is the normalized neutral–ion collision frequency. The parameters introduced above are the ion-to-electron temperature ratio $\sigma_i = \gamma_i T_i/T_e$, the neutral-to-electron temperature ratio $\sigma_n = \gamma_n T_n/T_e$, the dimensionless collision rates $\nu_{sn}^* = \nu_{sn}/\omega_{pi}$ for $s \in \{i, n\}$, and the dimensionless body-force parameter $G = g\lambda_D/C_s^2$, where g is the body-force acceleration along x, normalized by the characteristic acceleration scale C_s^2/λ_D. Here, T_i and T_n are the ion and neutral temperatures, respectively, while γ_i and γ_n are the effective polytropic indices of the ion and neutral fluids. Thus, σ_i and σ_n measure the normalized ion and neutral pressure responses relative to the electron thermal energy. In the numerical part of this study, we use the isothermal limit $\gamma_i = \gamma_n = 1$. Since Eqs. (3)–(4) are written in dimensionless form, the pressure-gradient terms, collision terms, and body-force term G all have consistent normalized units. The logarithmic derivatives, such as $\partial_x \ln n_i$ and $\partial_x \ln n_n$, are also dimensionless because x is normalized by the Debye length.

In the presence of a weak, uniform body force, for example gravity projected along x, the background satisfies specieswise hydrostatic balance. In the present normalization this reads [1]

$$\partial_x(\sigma_i n_{i0}) = -G\, n_{i0}, \tag{7}$$

$$\partial_x(\sigma_n n_{n0}) = -G\, n_{n0}. \tag{8}$$

Equations (7)–(8) integrate to exponential profiles

$$n_{i0}(x) \propto e^{-x/H_i}, \qquad n_{n0}(x) \propto e^{-x/H_n}, \qquad H_i = \frac{\sigma_i}{G}, \quad H_n = \frac{\sigma_n}{G}. \tag{9}$$

Here, $H_{i,n}$ are the dimensionless ion and neutral scale heights. Specifically, H_i and H_n denote the normalized scale heights of the ion and neutral background densities, respectively.

To incorporate altitude variation within a multiple-scale framework, we introduce the slow coordinate $X = \varepsilon x$ and assume $H_{i,n}^{-1} = O(\varepsilon)$, equivalently $G = O(\varepsilon)$, so that all coefficients vary weakly with X. The small parameter ε measures the asymptotically small perturbation amplitude and the slow spatial variation of the background, while X represents the slow coordinate associated with altitude-dependent plasma and neutral parameters. This gradually varying exponential background is consistent with conventional ionospheric aeronomy and lower-ionosphere constraints at Mars (M1) derived from Viking and MAVEN data [11, 18, 25].

Accordingly, the present formulation is restricted to a reduced asymptotic regime appropriate to the lower dayside Martian M1 ionosphere. In particular, we consider a one-dimensional electrostatic response with Boltzmann electrons, small-amplitude perturbations ordered within the standard reductive-perturbation expansion, and long wavelengths satisfying $k\lambda_D = O(\varepsilon^{1/2})$, so that dispersion and the leading nonlinear correction enter at the same asymptotic order. Here, k is the wavenumber of the electrostatic disturbance, so the condition $k\lambda_D = O(\varepsilon^{1/2})$ corresponds to a long-wavelength ordering relative to the Debye length. The small-amplitude qualification refers only to the asymptotic perturbation ordering and does not imply that the resulting solitary pulse is a linear or nearly linear structure. The background stratification is assumed weak through $H_{i,n}^{-1} = O(\varepsilon)$, while the ion–neutral collisional contribution is ordered so that the effective attenuation remains weak on the slow time scale. Under these assumptions, the model provides a reduced electrostatic description suitable for strongly collisional M1 conditions, while magnetic perturbations, plasma chemistry, and kinetic effects are beyond the scope of the present analysis.

3 Nonlinear analysis

We now apply the reductive perturbation method to the reduced electrostatic system introduced above, retaining Debye-length dispersion and slow background variation [26]. Let us introduce the stretched variables as

$$\xi = \varepsilon^{1/2}(x - \lambda t), \quad \tau = \varepsilon^{3/2} t, \quad X = \varepsilon x. \tag{10}$$

The exponents $\varepsilon^{1/2}$ and $\varepsilon^{3/2}$ are chosen so that the leading nonlinear correction and Debye-scale dispersion enter at the same asymptotic order. Here, ε is a small dimensionless ordering parameter, ξ is the stretched coordinate moving with the linear wave, τ is the slow evolution time, X is the slow background coordinate, and λ is the normalized linear phase speed of the electrostatic ion-acoustic mode. The variables x and t are the normalized space and time introduced in Section 2 [1].

The dependent variables are then expanded about the equilibrium state as

$$n_i = n_{i0}(X) + \varepsilon n_{1i} + \varepsilon^2 n_{2i} + \cdots, \quad u_i = \varepsilon u_1 + \varepsilon^2 u_2 + \cdots, \tag{11}$$

$$n_n = n_{n0}(X) + \varepsilon n_{1n} + \varepsilon^2 n_{2n} + \cdots, \quad u_n = \varepsilon w_1 + \varepsilon^2 w_2 + \cdots, \tag{12}$$

$$\phi = \phi_0(X) + \varepsilon \phi_1 + \varepsilon^2 \phi_2 + \cdots \tag{13}$$

In these expansions, n_{i0} and n_{n0} are the slowly varying equilibrium ion and neutral densities, respectively. The quantities n_{1i}, n_{2i}, n_{1n}, and n_{2n} are the first- and second-order ion and neutral density perturbations. Similarly, u_1 and u_2 are the first- and second-order ion velocity perturbations, while w_1 and w_2 are the corresponding neutral velocity perturbations. The quantities ϕ_0, ϕ_1, and ϕ_2 denote the equilibrium, first-order, and second-order normalized electrostatic potentials.

For small-amplitude disturbances, we use the expansions

$$\ln n_i = \ln n_{i0} + \varepsilon \frac{n_{1i}}{n_{i0}} + \varepsilon^2 \left(\frac{n_{2i}}{n_{i0}} - \frac{n_{1i}^2}{2n_{i0}^2} \right) + \cdots, \tag{14}$$

$$e^{\phi} = e^{\phi_0} \left[1 + \varepsilon \phi_1 + \varepsilon^2 \left(\phi_2 + \frac{1}{2}\phi_1^2 \right) + \cdots \right]. \tag{15}$$

These expansions are valid for $|n_{1i}|/n_{i0} = O(\varepsilon)$, $|\phi_1| = O(\varepsilon)$. In addition, with k describing the wavenumber of the electrostatic disturbance, the ordering $k\lambda_D = O(\varepsilon^{1/2})$ expresses the long-wavelength limit in which Debye-scale dispersion enters at the same asymptotic order as the leading nonlinear correction [26, 27].

The collision frequencies ν_{in}^* and ν_{ni}^* are ordered so that their contributions remain in the final evolution equation, i.e.

$$\nu_{in}^* = \varepsilon^{3/2} \tilde{\nu}, \quad \nu_{ni}^* = \varepsilon^{3/2} \tilde{\nu} \frac{m_i n_{i0}}{m_n n_{n0}}. \tag{16}$$

Here, ν_{in}^* and ν_{ni}^* are the normalized ion–neutral and neutral–ion collision frequencies, respectively, while $\tilde{\nu}$ is an order-unity scaled collision parameter. The factor $m_i n_{i0}/(m_n n_{n0})$ enforces momentum-transfer symmetry between the ion and neutral fluids.

Inserting the stretching relations (10) into the ion continuity equation (1) gives

$$-\lambda\, \partial_\xi n_{1i} + n_{i0}\, \partial_\xi u_1 = 0 \quad \Rightarrow \quad n_{1i} = \frac{n_{i0}}{\lambda}\, u_1. \tag{17}$$

At the lowest order, Poisson's equation with Boltzmann electrons, in the long-wavelength limit $k\lambda_D \ll 1$, gives

$$\phi_1 = \frac{n_{1i}}{n_{e0}} \simeq \frac{n_{1i}}{n_{i0}} = \frac{u_1}{\lambda}, \tag{18}$$

where the quasi-neutral character of the plasma has been used. Here, n_{e0} is the equilibrium electron density, and the approximation $n_{e0} \simeq n_{i0}$ follows from quasi-neutrality at leading order.

Substituting Eqs. (17)–(18) into the ion momentum equation at the same order results in the linear phase speed

$$\lambda = \sqrt{1+\sigma_i}. \tag{19}$$

This lowest-order result identifies the underlying linear ion-acoustic mode supported by the warm-ion, Boltzmann-electron plasma. The subsequent analysis extends this mode to finite but asymptotically small amplitudes, for which nonlinear steepening, Debye-scale dispersion, weak stratification, and ion–neutral attenuation act together. The solitary pulse remains intrinsically nonlinear; the small-amplitude qualification refers only to the asymptotic ordering used in the reductive-perturbation expansion. This distinction is important when assessing whether a localized electrostatic disturbance can remain coherent and observable in the strongly collisional M1 environment.

Combining the next higher-order contributions leads to the variable-coefficient Korteweg–de Vries equation with weak collisional attenuation

$$\Psi_\tau + \alpha\,\Psi\Psi_\xi + \beta\,\Psi_{\xi\xi\xi} + S\,\Psi_\xi + \boldsymbol{\Gamma_{\text{eff}}\,\Psi} = 0, \tag{20}$$

where $\Psi = \phi_1$, and the corresponding coefficients are defined as

$$\alpha = \frac{1+\gamma_i\sigma_i}{2}, \tag{21}$$

$$\beta = \frac{1}{2\sqrt{1+\sigma_i}}, \tag{22}$$

$$S = \frac{\lambda}{2}\,\partial_X \ln n_{i0}(X) = -\frac{\lambda}{2H_i}, \tag{23}$$

$$\Gamma_{\text{eff}} = \frac{\tilde{\nu}}{2}\,\frac{1}{1+\chi\,\mu\,\Lambda}, \tag{24}$$

$$\chi = \frac{n_{n0}}{n_{i0}}, \tag{25}$$

$$\mu = \frac{m_n}{m_i}, \tag{26}$$

$$\Lambda = \frac{\lambda^2}{\lambda^2+\sigma_n}. \tag{27}$$

The factor Λ is the neutral co-motion factor, measuring the degree to which neutrals participate in the pulse dynamics. In Eq. (20), Ψ is the first-order normalized electrostatic potential perturbation. The coefficient α measures nonlinear steepening, β measures Debye-scale dispersive spreading, S represents the drift produced by weak background stratification, and Γ_{eff} is the effective temporal attenuation rate caused by ion–neutral momentum exchange. The parameter χ is the neutral-to-ion equilibrium density ratio, μ is the neutral-to-ion mass ratio, and Λ measures the degree of neutral co-motion with the electrostatic pulse. The positive sign of the attenuation term in Eq. (20) is consistent with the decaying pulse amplitude derived below.

Before introducing the adiabatically evolving solitary-pulse solution, the validity of the weak-attenuation approximation must be specified. The characteristic amplitude-decay time in the slow coordinate is

$$\tau_{\mathrm{d}} = \frac{1}{2\Gamma_{\mathrm{eff}}}. \tag{28}$$

The characteristic time for the pulse to propagate over one initial width in the co-moving coordinate is

$$\tau_{\mathrm{p}} = \frac{\Delta_0}{V_0}, \qquad V_0 = \frac{\alpha\Phi_0(0)}{3}. \tag{29}$$

The attenuation is weak when the pulse amplitude changes only slightly during this characteristic pulse-evolution time, namely

$$\delta_{\mathrm{d}} \equiv \frac{\tau_{\mathrm{p}}}{\tau_{\mathrm{d}}} = \frac{2\Gamma_{\mathrm{eff}}\Delta_0}{V_0} = \frac{6\Gamma_{\mathrm{eff}}\Delta_0}{\alpha\Phi_0(0)} \ll 1. \tag{30}$$

For the representative values $\Phi_0(0) = 0.05$, $\alpha = 0.625$, and $\beta = 0.4472$, one obtains $\Delta_0 \simeq 13.10$ and $V_0 \simeq 1.04 \times 10^{-2}$. The fully co-moving case, $\Gamma_{\mathrm{eff}} = 2.5 \times 10^{-10}$, gives $\delta_{\mathrm{d}} \simeq 6.3 \times 10^{-7}$ and therefore satisfies the weak-attenuation condition. By contrast, the immobile-neutral upper-bound case, $\Gamma_{\mathrm{eff}} = 6.77 \times 10^{-4}$, gives $\delta_{\mathrm{d}} \simeq 1.7$, so the adiabatic solution is not quantitatively controlled in that limiting case. It is therefore retained only as a qualitative maximum-attenuation comparison.

For parameter regimes satisfying Eq. (30), the attenuation term can be treated as a slow perturbation of the nonlinear pulse evolution. For a localized initial condition in ξ, the electrostatic potential Ψ can be written as [28, 29]

$$\Psi(\xi,\tau) = \Phi_0(\tau)\,\mathrm{sech}^2\left(\frac{\xi - \xi_c(\tau)}{\Delta(\tau)}\right), \tag{31}$$

where the amplitude and width are time dependent and given by

$$\Phi_0(\tau) = \Phi_0(0)e^{-2\Gamma_{\mathrm{eff}}\tau}, \tag{32}$$

$$\Delta(\tau) = \sqrt{\frac{12\beta}{\alpha\Phi_0(\tau)}} = \Delta_0 e^{\Gamma_{\mathrm{eff}}\tau}, \tag{33}$$

$$\xi_c(\tau) = \eta_0 + S\tau + \frac{\alpha\Phi_0(0)}{6\Gamma_{\mathrm{eff}}}\left(1 - e^{-2\Gamma_{\mathrm{eff}}\tau}\right), \tag{34}$$

$$\Delta_0 = \sqrt{\frac{12\beta}{\alpha\Phi_0(0)}}. \tag{35}$$

Here, η_0 is the initial pulse position. The intrinsic pulse speed relative to the stratification drift is

The quantity $\Phi_0(\tau)$ given by Eq. (32) is the time-dependent pulse amplitude, $\Phi_0(0)$ is its initial value, $\Delta(\tau)$ is the time-dependent pulse width, Δ_0 is the initial width, $\xi_c(\tau)$ is the pulse-center position in the stretched coordinate, and η_0 is the initial pulse-center position in the co-moving frame. The quantity $V(\tau)$ denotes the intrinsic solitary-pulse speed in the co-moving coordinate. The details of the derivation of Eq. (31) are provided in the Appendix.

Equations (31)–(35) describe a solitary electrostatic pulse that slowly loses energy to the medium. The attenuation reduces the crest height, increases the pulse width, and slows the pulse down without immediately destroying the waveform. Instead, the pulse evolves adiabatically, with its parameters varying on a slower time scale than the waveform itself. The pulse position contains both a uniform drift associated with the stratification parameter S and a soliton self-motion that decreases as the amplitude decays. This adiabatic interpretation is quantitatively applicable only when the weak-attenuation criterion in Eq. (30) is satisfied.

To relate the stretched-coordinate description to physical scales, the slow time is connected to physical time by $t_{\rm phys} = \tau/(\varepsilon^{3/2}\omega_{pi})$, and a stretched width $\Delta(\tau)$ corresponds to a physical width $L_{\rm phys} = \lambda_D \varepsilon^{-1/2}\Delta(\tau)$. Similarly, the physical pulse-center position can be obtained from $x_{\rm phys} = \lambda_D x$, with $x = \lambda t + \varepsilon^{-1/2}\xi_c(\tau)$ and $t = \omega_{pi} t_{\rm phys}$. These relations allow the predicted amplitude decay, pulse broadening, and pulse motion to be interpreted in terms of observable temporal and spatial scales.

Physically, the coefficients α, β, and $\Gamma_{\rm eff}$ govern nonlinear steepening, dispersive spreading, and collisional attenuation, respectively. A larger α yields a narrower and faster pulse, a larger β produces a wider pulse, and a smaller $\Gamma_{\rm eff}$ allows the soliton to survive for a longer time. Therefore, this solution applies within the reduced weak-attenuation regime introduced above, where a coherent solitary pulse can survive long enough for its slow evolution to be resolved.

4 Results and Discussion

Before discussing the parameter dependence of the solitary structures, we first connect the results to the observational and physical motivation of the study. Direct waveform measurements in the lower dayside M1 region remain limited, while MAVEN/ROSE, LPW, NGIMS, and Viking measurements constrain the local plasma–neutral environment through electron-density profiles, *in situ* plasma diagnostics, neutral/ion composition, and lower-atmosphere composition data [10, 14, 18, 19]. The main question addressed here is, therefore, whether small-amplitude nonlinear electrostatic ion-acoustic solitary disturbances, if generated in this region, can survive the weakly ionized and strongly collisional M1 conditions, and which parameters control their amplitude, width, speed, lifetime, and possible detectability. The coefficients in the reduced evolution equation (20) provide the diagnostic link between the model and this question, following the standard reductive-perturbation/KdV interpretation of nonlinear, dispersive, stratification, and weak attenuation effects [26–29]. In Eq. (20), the coefficient α governs nonlinear steepening, β controls dispersive spreading, S represents the weak drift caused by background stratification, and $\Gamma_{\rm eff}$ determines the temporal attenuation caused by ion–neutral collisional relaxation. Thus, variations in α and β mainly determine the intrinsic pulse shape and propagation speed, whereas changes in S, $\Gamma_{\rm eff}$, and the neutral co-motion factor Λ determine the pulse drift, survival, and observability.

Here, we investigate small-amplitude nonlinear electrostatic ion-acoustic solitary waves that may form in the dayside M1 region of the Martian ionosphere. The small-amplitude qualification refers to the asymptotic ordering used in the reductive-perturbation analysis and not to the intrinsically nonlinear character of the resulting solitary pulse. Rather than assuming that these structures necessarily provide a dominant energy-transfer mechanism, we use the model to test whether such localized electrostatic disturbances can remain coherent under representative M1 plasma–neutral conditions. The analysis adopts plasma parameters derived from MAVEN observations. Observational data indicate that, in the dayside M1 region, the ion population is dominated by O_2^+ ($\sim$ 70–95%), with a smaller fraction of CO_2^+ ($\sim$ 3–20%). The neutral background is primarily composed of CO_2 ($\sim$ 85–99%), with additional contributions from O ($\sim$ 0.1–10%), CO ($\sim$ 0.1–5%), and the combined N_2+Ar fraction ($\sim$ 0.5–5%) [11, 18, 19, 25, 30, 31]. Using these inputs, our model focuses primarily on the O_2^+ ion population and the CO_2-dominated neutral background, so that $\mu \equiv m_n/m_i \simeq 1.375$, and we assume that $\gamma_i \simeq \gamma_n \simeq 1$ [1]. The plasma parameters representative of the dayside M1 transition region are listed in Table 1. The dayside M1 layer extends approximately from $\sim$ 90 to 135 km, and for the present analysis it is divided into five subregions, A_1–A_5. Each subregion is characterized by specific plasma parameters associated with ion-density irregularities, indicating that this layer exhibits significant dynamical variability. Using the physical parameters in Table 1, the corresponding coefficients $(\alpha, \beta, S, \Gamma_{\rm eff})$ are calculated and summarized in Table 2.

Figure 1 illustrates the altitude dependence of the electrostatic pulse profile, $\Psi(\xi, \tau)$, at two representative altitudes, A_1 (95 km) and A_5 (135 km). Panels (a)–(b) present snapshots of $\Psi(\xi, \tau)$ at several values of τ. In both cases, the pulse amplitude decreases while its width increases, consistent with the analytical laws $\Phi_0(\tau) = \Phi_0(0)e^{-2\Gamma_{\rm eff}\tau}$ and $\Delta(\tau) = \Delta_0 e^{\Gamma_{\rm eff}\tau}$. The decay is clearly stronger in the A_1 subregion than in the A_5 subregion. Panels (c)–(d) further show the normalized pulse amplitude and width as functions of τ. Figure 1 also indicates that, at 135 km, the lower neutral density n_n reduces $\tilde{\nu}$, leading to a smaller $\Gamma_{\rm eff}$ and therefore slower attenuation. In contrast, at 95 km, the higher n_n increases $\tilde{\nu}$, resulting in a larger $\Gamma_{\rm eff}$, faster amplitude loss, and stronger pulse broadening. It should also be noted that α and β vary only weakly with altitude through changes in σ_i, indicating that the temperature ratio does not play a dominant role in this altitude scan. The stratification drift, S, introduces only a small uniform shift of the pulse crest in ξ. Thus, the altitude scan mainly answers the survival part of the motivating question: electrostatic structures are expected to dissipate more rapidly in the lower M1 region and persist longer at higher M1 altitudes because collisional attenuation weakens as the neutral density decreases.

The characteristic frequency range associated with the electric pulses is estimated in Figure 2. Here, we consider both the temporal profile and its corresponding FFT power spectrum. Panels (a) and (b) show that the bipolar electric-field structure remains nearly unchanged from A_1 to A_5, with a peak amplitude of about $0.016 - 0.017$ mV m^{-1} and a duration of the order of 10^{-3} s. The FFT spectra indicate that most of the power is concentrated in the 6–7 kHz frequency range. These values provide the observationally relevant output of the model: the pulse duration controls the spectral scale, while the weak altitude dependence of the pulse shape produces only small differences in the high-frequency tail.

These waveform properties define specific observational targets for a future low-altitude Mars mission. Resolving a signal near 6–7 kHz requires an electric-field waveform receiver with a sampling rate above the corresponding Nyquist limit and, in practice, in the tens-of-kilohertz range. Because the predicted electric-field amplitude is weak, high instrumental sensitivity would also be required. Simultaneous measurements of electron density and temperature, ion composition, and neutral density and composition would allow the observed pulse properties and attenuation rate to be compared directly with the local plasma–neutral environment. The value of such a detection would therefore lie in using the pulse as a localized diagnostic of collisional relaxation and neutral co-motion in the M1 layer.

Our analysis shows that varying the neutral co-motion factor Λ does not influence the intrinsic balance of Eq. (20). The coefficients α, β, and S remain independent of Λ, while only the effective attenuation rate, Γ_{eff}, changes. This indicates that the neutral response mainly controls the long-time survival of the pulse. Increasing the co-motion between ions and neutrals reduces the effective ion–neutral drag by distributing the momentum transfer over a larger ion–neutral ensemble and therefore slows the decay of the electrostatic pulse. As shown in Table 3, the contrast between the L_0 and L_1 cases does not affect α, β, and S, but it alters the relaxation rate through Γ_{eff}. Figure 3 shows that this dependence becomes most apparent in the limiting cases. For immobile neutrals ($\Lambda = 0$), the pulse amplitude and velocity decay rapidly, while the width increases on a relatively short slow-time scale. In the fully co-moving case ($\Lambda = 1$), dissipation is strongly suppressed, the evolution becomes nearly adiabatic, and both amplitude decay and pulse broadening remain weak even up to very large τ. The coincidence of the normalized amplitude and speed curves follows directly from the relation $V(\tau) \propto \Phi_0$ (cf. Eq. (A16)), confirming that the dynamics remain self-consistent in both limiting regimes.

The weak-attenuation criterion introduced in Section 3 clarifies the validity of these two limiting regimes. For the representative initial pulse used in the calculations, the fully co-moving case gives $\delta_{\text{d}} \simeq 6.3 \times 10^{-7}$, so its adiabatic evolution is quantitatively consistent with the reduced solitary-pulse solution. By contrast, the immobile-neutral upper-bound case gives $\delta_{\text{d}} \simeq 1.7$ and therefore lies outside the quantitatively controlled adiabatic regime. Consequently, the immobile-neutral case is retained only as a qualitative maximum-attenuation comparison rather than as a quantitatively valid prediction of the pulse lifetime.

A physically useful outcome of this analysis is that the appropriate neutral treatment is determined by the ratio $R \equiv \nu_{in}/\omega$, where $\omega \simeq kC_s$. Large values of R correspond to the co-moving regime, while small R corresponds to the immobile-neutral limit. For intermediate values of R, the full two-fluid description is required. Applying this criterion to the Martian M1 region indicates that ion–neutral coupling weakens with altitude because the neutral density decreases rapidly. Therefore, for a fixed wavelength, lower M1 conditions are more likely to approach the co-moving regime, whereas upper M1 conditions may approach the immobile-neutral limit, especially for shorter and faster disturbances. Longer-wavelength disturbances, however, may remain more strongly coupled to the neutrals throughout the M1 region. In this sense, Λ acts as a practical diagnostic of dissipative control: it determines whether a localized electrostatic pulse undergoes rapid collisional decay or evolves more adiabatically. The present limiting analysis therefore identifies the range of possible behaviours rather than assigning a single universal neutral response to the whole M1 layer.

The values displayed in Table 4 show that changing $n_{i0} \simeq n_{e0}$ does not modify the nonlinear and dispersive coefficients, since α and β depend mainly on the temperature ratio σ_i. The ion/electron density affects the stratification drift through the Debye length, $\lambda_D \propto n_{e0}^{-1/2}$, and also modifies the effective attenuation rate. Although $\tilde{\nu} \propto n_{e0}^{-1/2}$ decreases as n_{e0} increases, the neutral loading parameter $\chi \propto n_{e0}^{-1}$ decreases more rapidly. Consequently, Eq. (24) gives $\Gamma_{\text{eff}} \propto n_{e0}^{1/2}$, so higher ion/electron density shortens the effective pulse lifetime.

The characteristic slow time for a 90% decrease of the pulse amplitude follows from Eq. (32) as

$$\tau_{90} = \frac{\ln 10}{2\Gamma_{\text{eff}}} \approx \frac{1.15}{\Gamma_{\text{eff}}}. \tag{37}$$

For the NI5 immobile-neutral upper-bound value $\Gamma_{\text{eff}} = 3.38 \times 10^{-4}$, this expression formally gives $\tau_{90} \simeq 3.41 \times 10^3$. At this time, the amplitude has decreased to $0.1\Phi_0(0)$, while the formal adiabatic expression gives a width increase to approximately $3.16\Delta_0$. To express this result in physical units, we use

$$t_{\text{phys}} = \frac{\tau}{\varepsilon^{3/2}\omega_{pi}}. \tag{38}$$

For $n_{i0} = 1 \times 10^{11}\,\text{m}^{-3}$, $m_i = 32m_p$, and $\omega_{pi} \simeq 7.36 \times 10^4\,\text{s}^{-1}$, taking $\varepsilon = 10^{-1}$ gives a formal physical time of approximately 1.46 s. However, because the immobile-neutral upper-bound case does not satisfy the weak-attenuation criterion, this value is interpreted only as an order-of-magnitude indication of strong collisional attenuation and not as a quantitatively controlled adiabatic solitary-pulse lifetime. Quantitative lifetime and detectability predictions are therefore restricted to parameter regimes satisfying $\delta_{\text{d}} \ll 1$.

Table 5 shows that ion temperature mainly controls the intrinsic nonlinear–dispersive balance rather than the long-time attenuation. As T_i increases, the warm-ion ratio σ_i increases, which strengthens the nonlinear coefficient and slightly reduces the dispersive coefficient. The resulting pulse is, therefore, narrower and faster at fixed amplitude. The decrease of β/α corresponds to a smaller initial width, while the increase in the intrinsic soliton speed reflects the stronger nonlinear contribution. In contrast, Γ_{eff} remains nearly unchanged across the considered T_i range, so the attenuation-controlled relaxation time is almost unaffected. As a result, ion temperature acts mainly as a structure-setting parameter, not as a survival-setting parameter.

The values listed in Table 6 show that, in the co-moving neutral model, changing the neutral density n_n does not alter the intrinsic nonlinear–dispersive balance of the electrostatic pulse. The coefficients α, β, and S remain fixed during the NN1–NN5 scan, so the basic pulse shape is essentially unchanged. The only affected coefficient is Γ_{eff}. However, in the co-moving regime, the increase of ion–neutral collision frequency with n_n is largely compensated by the increase of the neutral loading parameter $\chi \simeq n_n/n_e$, causing the net attenuation to remain nearly saturated. Thus, the density of the neutral species, n_n, is a weak control parameter in the co-moving limit, although it can become important in the immobile-neutral limit, where the attenuation increases more directly with neutral density.

Table 7 shows that neutral temperature produces only a weak modification of the pulse dynamics over the range considered. Since T_e and T_i are fixed, the nonlinear and dispersive coefficients remain unchanged, and the basic electrostatic pulse profile is almost unaffected. Neutral temperature enters mainly through the neutral co-motion response and, therefore, through Γ_{eff}. As T_n increases from 140 K to 220 K, Γ_{eff} increases only slightly, from 2.81×10^{-10} to 3.00×10^{-10}. Therefore, a higher neutral temperature produces only a marginally faster amplitude decay and pulse broadening. Within the present parameter range, neutral temperature does not significantly modify the nonlinear wave structure; its main effect is a small correction to the long-term attenuation behaviour.

Overall, our results distinguish between the parameters that determine pulse structure and those that determine observational survival. The intrinsic shape and speed are governed mainly by nonlinear and dispersive effects, whereas effective ion–neutral attenuation and neutral co-motion control whether the pulse persists long enough to be detected. The predicted bipolar electric-field amplitude, millisecond duration, kilohertz spectral range, and altitude-dependent attenuation provide testable signatures for a future low-altitude Mars mission. The present model does not claim a general theory for all Martian electrostatic structures; rather, it provides a data-constrained diagnostic for assessing whether small-amplitude nonlinear electrostatic ion-acoustic solitary structures can persist, broaden, or decay in the lower dayside Martian M1 ionosphere.

5 Summary and Conclusions

Our study addressed whether small-amplitude nonlinear electrostatic ion-acoustic solitary disturbances, if generated in the lower dayside Martian M1 ionosphere, can survive its weakly ionized and strongly collisional plasma–neutral environment. We derived a variable-coefficient Korteweg–de Vries equation with weak collisional attenuation from a multi-fluid Boltzmann–Poisson model for O_2^+ ions in a CO_2-dominated neutral background. The model includes warm-ion nonlinearity, Debye-scale dispersion, weak stratification, ion–neutral momentum exchange, and partial neutral co-motion. The reduced description is not presented as a new mathematical technique, but as an M1-specific diagnostic model constrained by representative MAVEN/Viking conditions. The small-amplitude qualification refers to the reductive-perturbation ordering and not to the intrinsically nonlinear character of the solitary pulse. The model therefore extends the conventional nonlinear ion-acoustic balance to a vertically structured and collisionally coupled lower-ionospheric environment in which the neutral response may substantially modify pulse evolution.

The intrinsic pulse shape and speed are controlled mainly by the nonlinear and dispersive coefficients, whereas pulse survival is controlled primarily by effective ion–neutral attenuation and neutral co-motion. More specifically, nonlinear steepening and dispersive spreading determine the amplitude–width and amplitude–speed relations, while effective ion–neutral attenuation controls the long-term decrease in pulse amplitude and the corresponding increase in pulse width. Attenuation is generally stronger in the denser lower M1 region and weaker at higher altitudes. Thus, altitude mainly controls pulse persistence rather than the intrinsic nonlinear–dispersive structure. Ion-density variation leaves this intrinsic balance nearly unchanged but modifies the stratification drift and effective attenuation through changes in the Debye length and neutral loading. Ion temperature controls pulse width and speed more strongly than lifetime, while neutral temperature has only a weak effect. Increasing the ion temperature strengthens nonlinear steepening and slightly reduces dispersion, producing narrower and faster pulses at fixed amplitude. By contrast, neutral-density variations have only a limited influence in the co-moving regime because the increase in collision frequency is largely compensated by the increasing neutral momentum reservoir, causing the effective attenuation to approach saturation.

The neutral co-motion factor is the most influential neutral parameter because it changes the effective attenuation by several orders of magnitude between the immobile-neutral and fully co-moving limits. The co-moving cases satisfy the weak-attenuation criterion and support a quantitatively controlled adiabatic pulse description, whereas the immobile-neutral case violates this criterion for the representative pulse considered and is therefore interpreted only as a qualitative maximum-attenuation bound. The intrinsic pulse speed also remains proportional to its amplitude, so the normalized speed and amplitude follow the same attenuation law. For the representative high-density immobile-neutral upper-bound case, the formal conversion to physical time indicates a ninety per cent amplitude reduction over approximately 1.46 seconds. Because this limiting case does not satisfy the weak-attenuation criterion, however, the estimated timescale is interpreted only as an order-of-magnitude indication of strong attenuation and not as a quantitatively controlled solitary-pulse lifetime.

The principal observational significance of the model is that the predicted solitary pulses may act as localized diagnostics of ion–neutral coupling and collisional relaxation. Their expected electric-field amplitude, duration, frequency range, altitude dependence, and attenuation behaviour provide measurable targets for a future low-altitude Mars mission. In particular, the predicted weak bipolar electric-field amplitude of approximately 0.016–0.017 millivolts per metre, millisecond duration, and spectral power near 6–7 kilohertz define specific waveform characteristics that could be searched for observationally. Such a mission would require high-sensitivity, high-cadence electric-field waveform measurements accompanied by simultaneous observations of electron density and temperature, ion composition, and neutral density and composition. These coordinated measurements would allow the observed pulse properties and attenuation rate to be compared directly with the local plasma–neutral coupling regime.

The present model is restricted to small-amplitude nonlinear, electrostatic, slowly varying disturbances in a strongly collisional environment and does not include magnetic perturbations, plasma chemistry, or kinetic effects. Accordingly, the conclusions are limited to the model-supported behaviour of electrostatic ion-acoustic solitary pulses in the lower Martian ionosphere. The results should therefore be interpreted as a diagnostic assessment of pulse formation and survival within the assumed fluid and weak-attenuation regimes, rather than as a general description of all electrostatic solitary structures in the Martian ionosphere. The model therefore provides a data-constrained framework for determining whether these disturbances are expected to persist, broaden, or decay under typical Martian M1 conditions and for identifying the observational requirements needed to test these predictions.

Appendix: Derivation of the solution given by (31)

We start our derivation from the KdV equation ((20)). To remove the drift term from this equation, we introduce the moving coordinate:

$$\eta = \xi - S\tau, \qquad \Phi(\eta, \tau) = \Psi(\xi, \tau), \tag{A1}$$

which shifts the description to a frame moving with the background shift S. In this frame, Eq. (20) reduces to

$$\Phi_\tau + \alpha\Phi\Phi_\eta + \beta\Phi_{\eta\eta\eta} - \Gamma_{\text{eff}}\Phi = 0. \tag{A2}$$

In the undamped limit, $\Gamma_{\text{eff}} = 0$, Eq. (A2) becomes the standard KdV equation. Its localized traveling-wave solution is

$$\Phi(\eta, \tau) = \Phi_0 \,\text{sech}^2\left(\frac{\eta - \eta_c}{\Delta}\right). \tag{A3}$$

We introduce the traveling-wave variable $\zeta = \eta - V\tau$ and set $\Phi(\eta, \tau) = F(\zeta)$, which reduces the equation, after one integration under localized boundary conditions, to

$$-VF + \frac{\alpha}{2}F^2 + \beta F'' = 0. \tag{A4}$$

Assuming the standard soliton profile $F(\zeta) = \Phi_0 \text{sech}^2(\zeta/\Delta)$, substitution into Eq. (A4) yields

$$\left(-V + \frac{4\beta}{\Delta^2}\right)F + \left(\frac{\alpha}{2} - \frac{6\beta}{\Phi_0\Delta^2}\right)F^2 = 0. \tag{A5}$$

Requiring the coefficients of F and F^2 to vanish gives the width-amplitude and speed-amplitude relations:

$$\Delta = \left(\frac{12\beta}{\alpha\Phi_0}\right)^{1/2}, \qquad V = \frac{d\eta_c}{d\tau} = \frac{\alpha\Phi_0}{3}. \tag{A6}$$

When damping is weak, we assume that the pulse retains its sech^2 shape but its parameters change slowly with τ; this is referred to as the *adiabatic approximation*, i.e., damping is changing with the parameters, not its shape. This requires a *time-dependent* solitary wave ansatz:

$$\Phi(\eta, \tau) = \Phi_0(\tau)\, \text{sech}^2\left(\frac{\eta - \eta_c(\tau)}{\Delta(\tau)}\right), \tag{A7}$$

where $\Phi_0(\tau)$, $\Delta(\tau)$, and $\eta_c(\tau)$ vary slowly compared with the fast spatial structure of the pulse.

To determine the amplitude evolution, we define the pulse area,

$$\mathcal{M}(\tau) = \int_{-\infty}^{\infty} \Phi(\eta, \tau)\, d\eta, \tag{A8}$$

i.e., the total area under the localized pulse profile. This quantity is particularly useful because, upon integration of Eq. (A3) over η, the nonlinear and dispersive contributions vanish under the localized boundary conditions, resulting in a closed evolutionary equation for $\mathcal{M}$ as

$$\frac{\mathrm{d}\mathcal{M}}{\mathrm{d}\tau} = -\Gamma_{\text{eff}}\mathcal{M}. \tag{A9}$$

For the profile in Eq. (A3),

$$\mathcal{M} = \Phi_0 \int_{-\infty}^{\infty} \operatorname{sech}^2\left(\frac{\eta - \eta_c}{\Delta}\right) d\eta = 2\Phi_0\Delta. \tag{A10}$$

Using Eq. (A6), this becomes

$$\mathcal{M} = 2\left(\frac{12\beta}{\alpha}\right)^{1/2} \Phi_0^{1/2}. \tag{A11}$$

Substitution into Eq. (A9) gives

$$\frac{\mathrm{d}\Phi_0}{\mathrm{d}\tau} = -2\Gamma_{\text{eff}}\Phi_0, \tag{A12}$$

and hence

$$\Phi_0(\tau) = \Phi_0(0)e^{-2\Gamma_{\text{eff}}\tau}. \tag{A13}$$

The width and intrinsic speed follow directly from Eq. (A6):

$$\Delta(\tau) = \Delta_0 e^{\Gamma_{\text{eff}}\tau}, \qquad \Delta_0 = \left(\frac{12\beta}{\alpha\Phi_0(0)}\right)^{1/2}, \tag{A14}$$

$$V(\tau) = \frac{\alpha}{3}\Phi_0(\tau) = \frac{\alpha}{3}\Phi_0(0)e^{-2\Gamma_{\text{eff}}\tau}. \tag{A15}$$

Since $d\eta_c/d\tau = V(\tau)$, integration gives

$$\eta_c(\tau) = \eta_0 + \frac{\alpha\Phi_0(0)}{6\Gamma_{\text{eff}}}\left(1 - e^{-2\Gamma_{\text{eff}}\tau}\right), \tag{A16}$$

Transforming back to the original coordinate, $\xi = \eta + S\tau$, the pulse center becomes

$$\xi_c(\tau) = \eta_0 + S\tau + \frac{\alpha\Phi_0(0)}{6\Gamma_{\text{eff}}}\left(1 - e^{-2\Gamma_{\text{eff}}\tau}\right). \tag{A17}$$

Therefore, the weakly damped solitary-wave solution is

$$\Psi(\xi,\tau) = \Phi_0(0)e^{-2\Gamma_{\text{eff}}\tau} \operatorname{sech}^2\left(\frac{\xi - \xi_c(\tau)}{\Delta_0 e^{\Gamma_{\text{eff}}\tau}}\right), \tag{A18}$$

which constitutes the solution given by Eq. (31).

Funding

This research work was funded by Umm Al-Qura University, Saudi Arabia under grant number 26UQU4340344GSSR01

Acknowledgments

The authors extend their appreciation to Umm Al-Qura University, Saudi Arabia for funding this research work through grant number 26UQU4340344GSSR01.

Declaration of competing interest

The authors declare that they have no known competing financial interests or personal relationships that could have appeared to influence the work reported in this paper.

Data availability

All data that support the findings of this study are included within the article.

References

[1] R. W. Schunk and A. F. Nagy, *Ionospheres: Physics, Plasma Physics, and Chemistry*, 2nd ed. (Cambridge University Press, 2009).

[2] T. E. Cravens, *Physics of Solar System Plasmas* (Cambridge University Press, 1997).

[3] T. V. Zaqarashvili, M. L. Khodachenko, and H. O. Rucker, Astronomy & Astrophysics **529**, A82 (2011).

[4] R. Soler *et al.*, Frontiers in Astronomy and Space Sciences **9**, 789083 (2022).

[5] K. R. Tripathi *et al.*, Geophysical Research Letters **49**, e2022GL097824 (2022).

[6] L. Rosenqvist, J.-E. Wahlund, K. Ågren, *et al.*, Planetary and Space Science **57**, 1828 (2009).

[7] C. Goetz, K. L. Heritier, G. H. Jones, *et al.*, Space Science Reviews **218**, 56 (2022).

[8] E. Vigren, M. Galand, *et al.*, Monthly Notices of the Royal Astronomical Society **482**, 1937 (2019).

[9] J. H. Waite *et al.*, Science **311**, 1419 (2006).

[10] P. Withers, M. Felici, M. Mendillo, L. Moore, C. Narvaez, M. Vogt, and B. Jakosky, Journal of Geophysical Research: Space Physics **123**, 4171 (2018).

[11] P. Withers, Advances in Space Research **44**, 277 (2009).

[12] K. Fallows, P. Withers, and M. Matta, Journal of Geophysical Research: Space Physics **120**, 1299 (2015).

[13] K. Peter, M. Pätzold, G. J. Molina-Cuberos, *et al.*, Icarus **359**, 114213 (2021).

[14] L. Andersson, R. E. Ergun, G. T. Delory, *et al.*, Space Science Reviews **195**, 173 (2015).

[15] M. Felici, P. Withers, N. Putzig, *et al.*, Journal of Geophysical Research: Space Physics **127**, e2021JA030155 (2022).

[16] D. J. Andrews, L. Andersson, G. T. Delory, *et al.*, Geophysical Research Letters **42**, 8862 (2015).

[17] C. M. Fowler *et al.*, Geophysical Research Letters **44**, 10845 (2017).

[18] P. R. Mahaffy, M. Benna, M. Elrod, R. Yelle, *et al.*, Space Science Reviews **195**, 49 (2015).

[19] A. O. Nier and M. B. McElroy, Science **194**, 1298 (1976).

[20] B. Kakad, A. Kakad, H. Aravindakshan, and I. Kourakis, The Astrophysical Journal **934**, 126 (2022).

[21] S. S. Varghese, K. Singh, F. Verheest, and I. Kourakis, The Astrophysical Journal **977**, 100 (2024).

[22] K. Singh, S. S. Varghese, and I. Kourakis, Scientific Reports **15**, 14506 (2025).

[23] I. S. Elkamash, R. Sabry, and W. M. Moslem, The European Physical Journal Plus **140**, 831 (2025).

[24] N. Chakraborty, S. Devanandhan, S. Singh, and G. S. Lakhina, The Astrophysical Journal **997**, 198 (2026).

[25] M. Benna, P. R. Mahaffy, J. M. Grebowsky, J. L. Fox, and B. M. Jakosky, Geophysical Research Letters **42**, 8958 (2015).

[26] H. Washimi and T. Taniuti, Physical Review Letters **17**, 996 (1966).

[27] A. H. Nayfeh, *Perturbation Methods* (John Wiley & Sons, New York, 1973).

[28] I. Ballai, J. C. Thelen, and B. Roberts, Astron. Astrophys. **404**, 701 (2003).

[29] I. Ballai, E. Forgács-Dajka, and A. Marcu, Advances in Space Research **63**, 1472 (2019), arXiv:1810.07948 [astro-ph.SR] .

[30] P. R. Mahaffy, M. Benna, M. Elrod, R. Yelle, *et al.*, Geophysical Research Letters **42**, 8951 (2015).

[31] J. L. Fox, Icarus **363**, 114421 (2021).

List of Figures

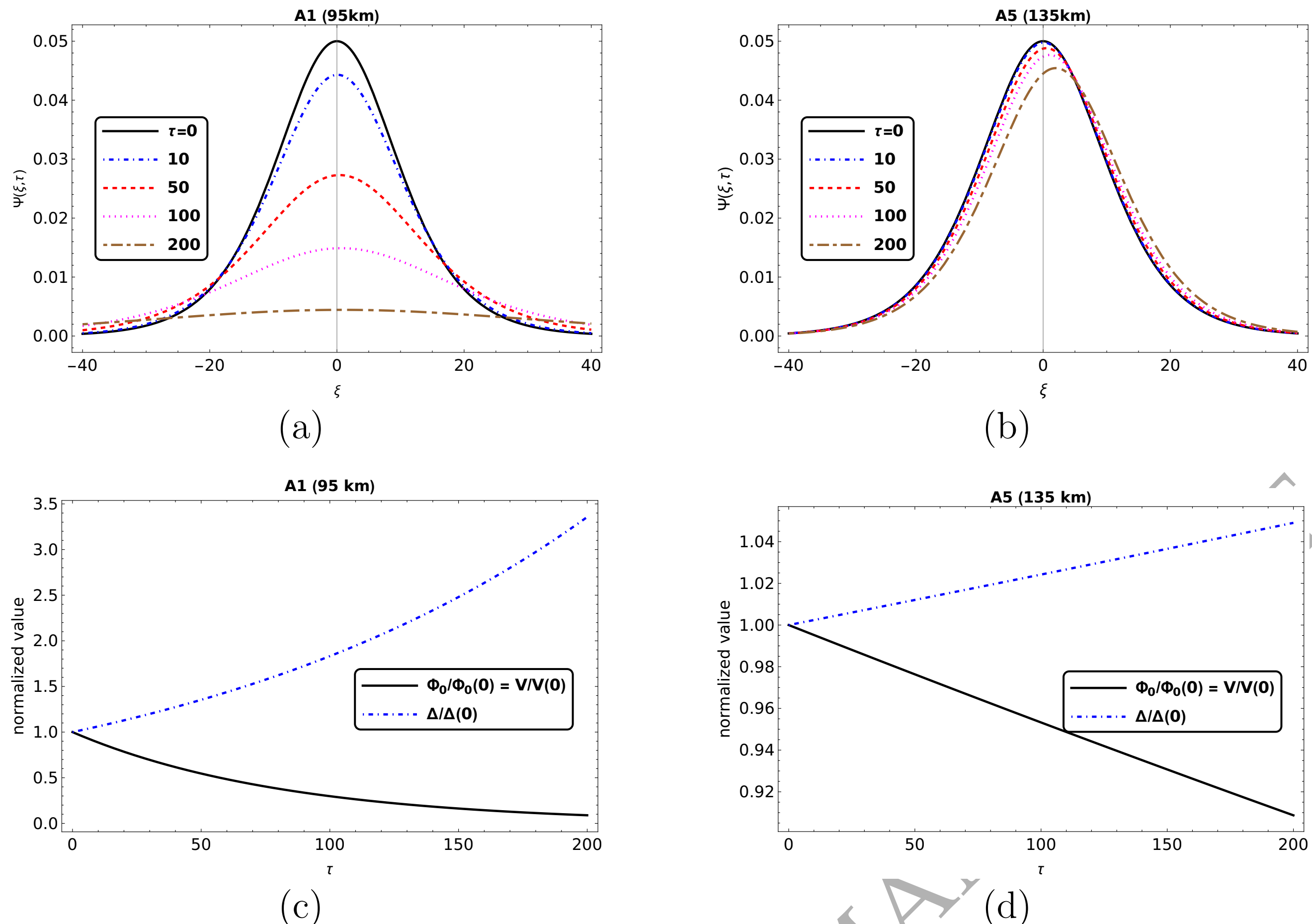

Figure 1: (Color online) Altitude dependence of weakly damped KdV solitary structures in the Martian dayside M1 region. (a–b) Snapshots of the normalized potential envelope $\Psi(\xi,\tau)$ at $\tau = 0, 10, 50, 100, 200$ for A1 (95 km) and A5 (135 km). (c–d) Normalized measures versus τ: $\Phi_0(\tau)/\Phi_0(0) = V(\tau)/V(0)$ and $\Delta(\tau)/\Delta(0)$.

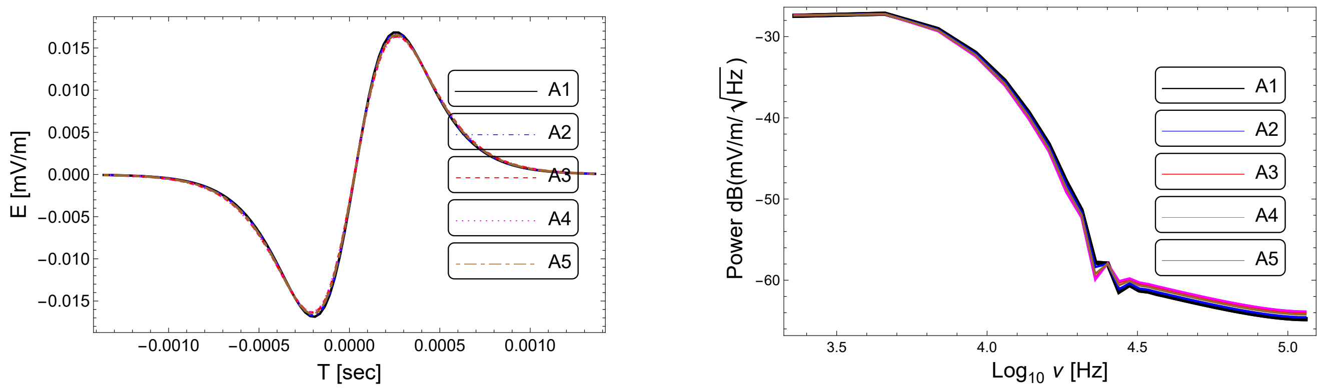

(a) (b)

Figure 2: (a) Electric field profile for altitude dependence of the plasma system parameters (see Table 1) and (b) the FFT power spectra of the electric field. The x-axis signifies the $\log_{10}\nu$, where ν is the frequency in Hz, and the y-axis represents the power of the electric field in units of dB(mV/m/Hz).

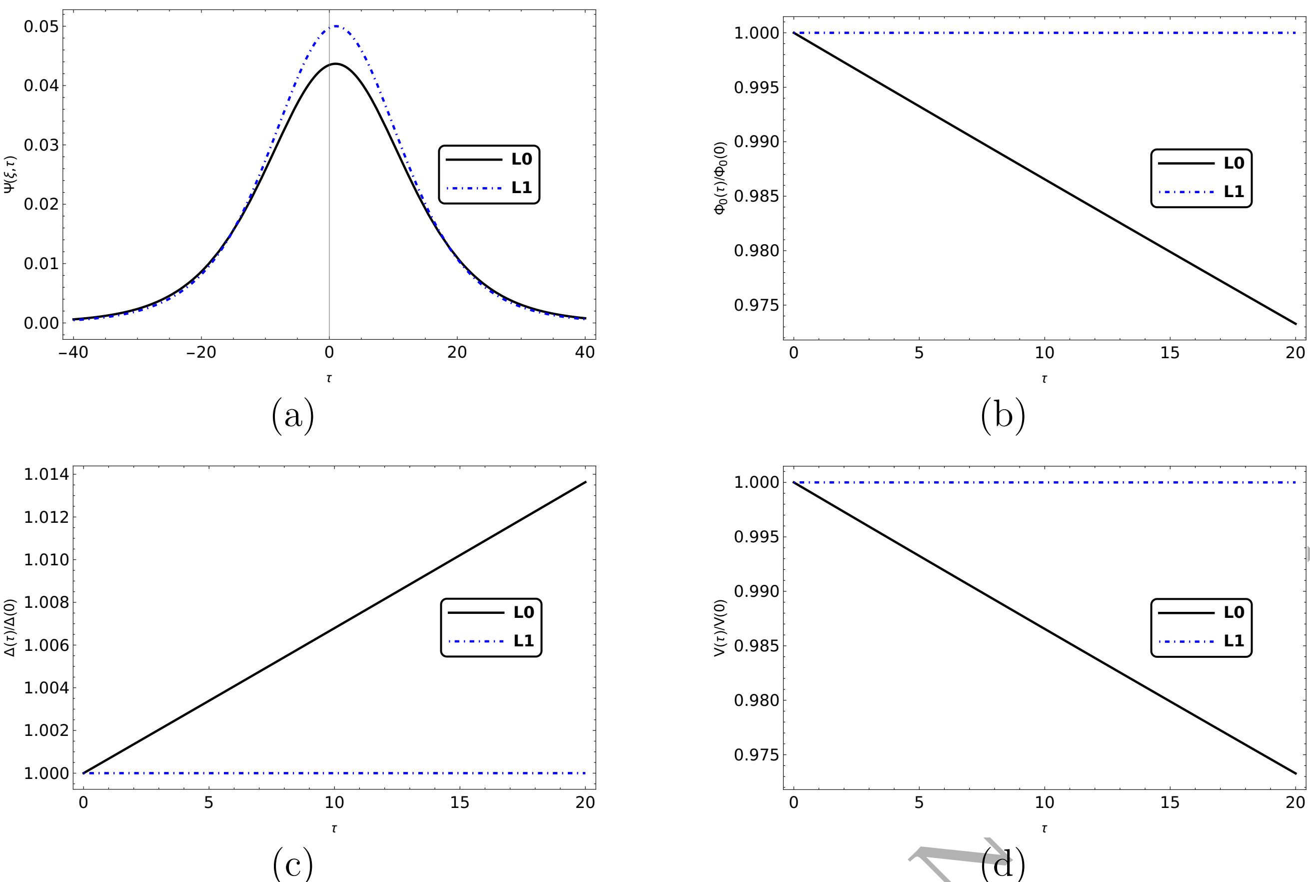

Figure 3: (Color online) Effect of neutral co–motion on soliton evolution at the $\sim$ 115 km baseline. Curves compare the immobile–neutral limit L0 ($\Lambda = 0$) and the cold, co–moving limit L1 ($\Lambda = 1$). (a) Representative profiles $\Psi(\xi, \tau)$ at selected τ. (b–d) Normalized amplitude $\Phi_0(\tau)/\Phi_0(0)$, width $\Delta(\tau)/\Delta(0)$, and intrinsic speed $V(\tau)/V(0)$ versus τ.

List of Tables

Table 1: Dayside M1 inputs by altitude (representative values).

Case	Alt. (km)	T_e [K]	T_i [K]	T_n [K]	n_e ($\simeq n_i$)$[m^{-3}]$	n_n [m^{-3}]
A1	95	600	180	170	5×10^9	2×10^{17}
A2	105	700	200	180	1.5×10^{10}	1×10^{17}
A3	115	800	200	180	2.5×10^{10}	5×10^{16}
A4	125	900	220	190	1.5×10^{10}	2×10^{16}
A5	135	1000	250	200	8×10^9	1×10^{16}

Sources: T_e, n_e and wave context from MAVEN/LPW; ROSE radio-occultation density profiles [10, 14, 15]. Neutrals from MAVEN/NGIMS (dayside) and Viking composition [18, 19, 30].

Table 2: Derived KdV coefficients and auxiliary scales (from Table 1).

Case	Alt. (km)	α	β	S	$\Gamma_{\rm eff}$
A1	95	0.650	0.439	-1.08×10^{-6}	1.34×10^{-10}
A2	105	0.643	0.441	-8.90×10^{-7}	2.29×10^{-10}
A3	115	0.625	0.447	-7.79×10^{-7}	2.90×10^{-10}
A4	125	0.622	0.448	-7.60×10^{-7}	2.23×10^{-10}
A5	135	0.625	0.447	-7.37×10^{-7}	1.62×10^{-10}

Table 3: KdV coefficients under the two bounding limits of the neutral co-motion factor Λ (dayside M1, $\sim$115 km baseline).

Case	Λ	Interpretation	α	β	S	$\Gamma_{\rm eff}$
L0	0	Immobile neutrals (max. damping)	0.6250	0.4472	-4.93×10^{-7}	6.77×10^{-4}
L1	1	Cold, co–moving neutrals (min. damping)	0.6250	0.4472	-4.93×10^{-7}	2.5×10^{-10}

Baseline (fixed): $T_e = 800\,$K; $T_i = 200\,$K; $T_n = 180\,$K; $n_e = 2.5 \times 10^{10}\,$m^{-3}; $n_n = 5 \times 10^{16}\,$m^{-3}; $k_{in} = 10^{-9}\,$cm$^3\,$s^{-1}; ion O_2^+ ($m_i = 32\,m_u$); neutral CO_2 ($m_n = 44\,m_u$); $\gamma_i = \gamma_n = 1$. Coefficients (independent of Λ): $\sigma_i = 0.25$; $\lambda = 1.118$; $\alpha = 0.625$; $\beta = 0.447$; $S = -4.93 \times 10^{-7}$. Other fixed factors: $\chi \approx 2 \times 10^6$; $\mu = 1.375$. Effective damping: L0 ($\Lambda = 0$) $\Gamma_{\rm eff} \approx 6.77 \times 10^{-4}$; L1 ($\Lambda = 1$) $\Gamma_{\rm eff} \approx 2.5 \times 10^{-10}$.

Table 4: KdV coefficients vs. ion density.

Case	n_i ($\simeq n_e$) [m^{-3}]	α	β	S	Γ_{eff}
NI1	5×10^{9}	0.625	0.447	-1.10×10^{-6}	1.30×10^{-10}
NI2	1×10^{10}	0.625	0.447	-7.79×10^{-7}	1.84×10^{-10}
NI3	2.5×10^{10}	0.625	0.447	-4.93×10^{-7}	2.90×10^{-10}
NI4	5×10^{10}	0.625	0.447	-3.48×10^{-7}	4.11×10^{-10}
NI5	1×10^{11}	0.625	0.447	-2.46×10^{-7}	5.81×10^{-10}

Common setup (all rows): O_2^+ ions; CO_2 neutrals; $T_e = 800$ K; $T_i = 200$ K; $T_n = 180$ K; $n_n = 5 \times 10^{16}\ \mathrm{m}^{-3}$; $k_{in} = 10^{-9}\ \mathrm{cm}^3\,\mathrm{s}^{-1}$; $\gamma_i = \gamma_n = 1$. Fixed coefficients/parameters: $\sigma_i = 0.25$; $\lambda = 1.118$; $\alpha = 0.625$; $\beta = 0.447$; $\sigma_n = 0.225$; $\mu = 1.375$. Immobile–neutral upper bound values ($\Gamma_{\mathrm{eff}}^{(\mathrm{imm.})}$): NI1 $= 1.51 \times 10^{-3}$; NI2 $= 1.07 \times 10^{-3}$; NI3 $= 6.77 \times 10^{-4}$; NI4 $= 4.79 \times 10^{-4}$; NI5 $= 3.38 \times 10^{-4}$.

Table 5: KdV coefficients vs. ion temperature T_i (dayside M1, ∼115 km baseline; only T_i varies).

Case	T_i [K]	α	β	S	Γ_{eff}
T1	150	0.5938	0.4588	-6.40×10^{-7}	2.93×10^{-10}
T2	180	0.6125	0.4518	-5.42×10^{-7}	2.91×10^{-10}
T3	200	0.6250	0.4472	-4.93×10^{-7}	2.90×10^{-10}
T4	240	0.6500	0.4385	-4.19×10^{-7}	2.89×10^{-10}
T5	300	0.6875	0.4264	-3.44×10^{-7}	2.86×10^{-10}

Baseline (∼115 km, A3): $T_e = 800\,\mathrm{K}$; $T_n = 180\,\mathrm{K}$; $n_e = 2.5 \times 10^{10}\,\mathrm{m^{-3}}$; $n_n = 5 \times 10^{16}\,\mathrm{m^{-3}}$; $k_{in} = 10^{-9}\,\mathrm{cm^3\,s^{-1}}$; ion O_2^+ ($m_i = 32\,m_u$); neutral CO_2 ($m_n = 44\,m_u$); $\gamma_i = \gamma_n = 1$. Immobile–neutral upper bound: $\Gamma_{\mathrm{eff}}^{(\mathrm{imm})} \approx 6.77 \times 10^{-4}$.

Table 6: KdV coefficients versus neutral density n_n (dayside M1, ∼115 km baseline; only n_n varies).

Case	n_n [m^{-3}]	α	β	S	Γ_{eff}
NN1	1.0×10^{16}	0.6250	0.4472	-4.93×10^{-7}	3.07×10^{-10}
NN2	3.0×10^{16}	0.6250	0.4472	-4.93×10^{-7}	3.07×10^{-10}
NN3	5.0×10^{16}	0.6250	0.4472	-4.93×10^{-7}	3.07×10^{-10}
NN4	1.0×10^{17}	0.6250	0.4472	-4.93×10^{-7}	3.07×10^{-10}
NN5	2.0×10^{17}	0.6250	0.4472	-4.93×10^{-7}	3.07×10^{-10}

Baseline (fixed): $T_e = 800\,\mathrm{K}$; $T_i = 200\,\mathrm{K}$; $T_n = 180\,\mathrm{K}$; $n_e = 2.5 \times 10^{10}\,\mathrm{m}^{-3}$; $k_{in} = 10^{-9}\,\mathrm{cm}^3\,\mathrm{s}^{-1}$; ion O_2^+ ($m_i = 32\,m_u$); neutral CO_2 ($m_n = 44\,m_u$); $\gamma_i = \gamma_n = 1$. Coefficients (independent of n_n): $\sigma_i = 0.25$; $\lambda = 1.118$; $\alpha = 0.625$; $\beta = 0.447$. Immobile–neutral upper bound $\Gamma_{\mathrm{eff}}^{(\mathrm{imm})}$: NN1 1.43×10^{-4}, NN2 4.30×10^{-4}, NN3 7.16×10^{-4}, NN4 1.43×10^{-3}, NN5 2.86×10^{-3}.

Table 7: KdV coefficients versus neutral temperature T_n (dayside M1, $\sim$115 km baseline; only T_n varies).

Case	T_n [K]	α	β	S	Γ_{eff}
N1	140	0.6250	0.4472	-4.93×10^{-7}	2.81×10^{-10}
N2	160	0.6250	0.4472	-4.93×10^{-7}	2.86×10^{-10}
N3	180	0.6250	0.4472	-4.93×10^{-7}	2.90×10^{-10}
N4	200	0.6250	0.4472	-4.93×10^{-7}	2.95×10^{-10}
N5	220	0.6250	0.4472	-4.93×10^{-7}	3.00×10^{-10}

Baseline (fixed): $T_e = 800\,\text{K}$; $T_i = 200\,\text{K}$; $n_e = 2.5 \times 10^{10}\,\text{m}^{-3}$; $n_n = 5 \times 10^{16}\,\text{m}^{-3}$; $k_{in} = 10^{-9}\,\text{cm}^3\,\text{s}^{-1}$; ion O_2^+ ($m_i = 32\,m_u$); neutral CO_2 ($m_n = 44\,m_u$); $\gamma_i = \gamma_n = 1$. Coefficients (independent of T_n): $\sigma_i = 0.25$; $\lambda = 1.118$; $\alpha = 0.625$; $\beta = 0.447$; $S = -4.93 \times 10^{-7}$. Other fixed factors: $\chi = 2 \times 10^6$; $\mu = 1.375$. Immobile–neutral upper bound: $\Gamma_{\text{eff}}^{(\text{imm})} \approx 6.77 \times 10^{-4}$.